Quantification of erosion pattern using Picosecond-LIBS on a vertical divertor target element exposed in W7-X

D. Zhao [a, b], R. Yi [a], A. Eksaeva [a], J. Oelmann [a], S. Brezinsek [a, *], G. Sergienko [a], M. Rasinski [a], Y. Gao [a], M. Mayer [c], C. P. Dhard [d], D. Naujoks [d], L. Cai [b], and the W7-X team [d]

[a]*Forschungszentrum Jülich, Institut für Energie- und Klimaforschung - Plasmaphysik, Partner of the Trilateral Euregio Cluster (TEC), 52425 Jülich, Germany*
[b]*Southwestern Institute of Physics, P.O.Box 432, Chengdu, Sichuan, 610041, China*
[c]*Max-Planck-Institut für Plasmaphysik, 85748 Garching, Germany*
[d]*Max-Planck-Institut für Plasmaphysik, 17491 Greifswald, Germany*

A B S T R A C T

A set of dedicated marker samples consisting of fine-grain graphite as substrate, an interlayer of 0.2–0.4 μm Molybdenum (Mo) employed as marker, and a 5-10 μm thick carbon (C) marker layer on top were installed in Wendelstein 7-X (W7-X) to investigate locally the C erosion and deposition. In this study, a set of five individual marker tiles, installed in a vertical divertor element of the Test Divertor Unit (TDU) in Half-Module 50 (HM50), and exposed to about 40 minutes of plasma predominant in the standard magnetic divertor configuration in the first year of divertor operation in W7-X (OP1.2A), were retrieved from the vessel for post-mortem analysis. Picosecond Laser Induced Breakdown Spectroscopy (ps-LIBS) was applied on these marker tiles in order to determine the local erosion/deposition pattern caused by plasma impact. The general erosion/deposition pattern on the vertical target element was studied with the aid of depth-profiling by Mo line emission due to ps-LIBS with the number of applied laser pulses (355 nm, 2.3 J/cm^2, 35 ps) at one probing location. Several potential asymmetry factors which avoid a perfect layer-by-layer ablation process in the laser ablations are proposed and discussed when a rough layered structure sample with a rough surface is analysed by the ps-LIBS technique. Thereby, a simulation model was developed to correct the measurement error of the ps-LIBS method caused by the non-perfect rectangle profile of the applied laser beam. The depth resolution of the applied ps-LIBS system was determined by quantification of the laser ablation rates of the different layers and the C substrate which were measured utilising profilometry and cross comparison with the thicknesses of the C and Mo marker layers determined by a combined Focused Ion Beam and Scanning Electron Microscopy (FIB-SEM) technique. For the first time, the erosion/deposition pattern on the vertical target was mapped and quantified by ps-LIBS technique. A relatively wide net erosion zone with a poloidal extend of about 200 mm was identified which can be correlated to the main particle interaction zone at the magnetic strike-line of the dominantly applied standard magnetic divertor configuration. At the position of peak erosion, not only 7.6×10^{19} C atoms/cm^2 but also 2×10^{18} Mo atoms/cm^2 which results can be extrapolated to total 15×10^{19} C atoms/cm^2, were eroded due to plasma fuel particle (H, He) and impurity (O, C) ion impact.

1. Introduction

The investigation of Plasma-Wall Interactions (PWI) in W7-X is challenging due to the complex three-dimensional helical plasma geometry and the large size of the graphite Plasma-Facing Components (PFCs) in the island divertor [1]. Full understanding of PWI, such as fuel retention, materials erosion and deposition, are among the crucial tasks for W7-X on the way towards a steady state fusion reactor, since these questions determine largely the fuel cycle, the lifetimes of the PFCs and the impurity influx [2]. For this purpose, several specially designed marker PFCs, installed in the uncooled graphite Test Divertor Unit (TDU) of W7-X as exchangeable target elements, were exposed to a combination of hydrogen (H) and helium (He) plasmas in order to investigate the local C erosion and deposition [3]. These dedicated marker samples consist of three layers: fine-grain graphite as substrate, an intermediate layer of 0.2–0.4 μm Mo, employed as marker, and on top a 5-10 μm thick C marker layer. These markers on the samples with a typical roughness of a few micrometers were produced by Combined-Magnetron Sputtering with Ion Implantation (CMSII) and act as part of the divertor target elements [4, 5]. In the W7-X Operation Phase (OP) 1.2A, the TDU was exposed to H and He plasmas with a total plasma time of 3776 seconds [6], of which 2481 s were carried out in the so-called standard divertor configuration and 714 s in the so-called high mirror configuration. Details about the magnetic configurations and associated particle and heat loads were further described in [7].

Laser-induced breakdown spectroscopy (LIBS) as a versatile tool for the investigation of the chemical composition of bulk materials is a potential candidate for *in-situ* investigations of PWI in nuclear fusion devices [8, 9]. Moreover, LIBS also has great potential for depth analysis of

Keywords: W7-X Divertor, erosion pattern, picosecond LIBS, quantitative analysis, layered sample
* Corresponding author. *E-mail address*: s.brezinsek@fz-juelich.de

multilayer samples based on laser ablation and atomic emission spectroscopy [10]. With these special benefits, LIBS had been installed in several tokamak devices and proposed for future application in W7-X for PWI research including fuel retention and erosion/deposition studies [11-16].

In our previous work, target elements of the horizontal divertor plate from the upper half module in sector 1, the so-called HM11 (**H**alf-**M**odule, sector **1**, and upper location **1**), were analysed in poloidal direction by a combination of ex-situ picosecond-LIBS (ps-LIBS) and Laser-Induced Ablation-Quadrupole Mass Spectrometry [17]. The results revealed an erosion-dominated area close to the location of the strike line in the standard island divertor configuration of W7-X with magnetic edge transformation ι=5/5. Moreover, the erosion pattern was in *qualitative* agreement with the heat flux distribution, measured in-situ by infrared (IR) thermography, and the erosion pattern measured complementary ex-situ by Elastic Backscattering Spectrometry (EBS) [6, 18]. However, the *quantification* of the erosion/deposition pattern using the ps-LIBS method on the W7-X graphite divertor tiles has not yet been addressed in our previous study.

In this work, the erosion/deposition pattern of the vertical target element TM2v2, which is located at HM50 of the TDU in W7-X, was analysed ex-situ using the ps-LIBS. W7-X is a stellarator with five-fold symmetry and equipped with a so-called island divertor design [19], consisting of an upper and lower divertor half module in each of the five sectors. The analysed divertor half module HM50 is located at the lower position marked by the **0** in the name. Further information about the divertor design and the flux tubes in plasma operation can be found in [20]. Depth profiling of the Mo marker layer was applied to determine the variation of erosion and deposition in poloidal direction due to plasma impact in OP1.2A. Three typical scan lines of ps-LIBS in toroidal direction with the line distance of 10 mm on the marker area of the target element were studied to examine erosion and deposition. Moreover, a combination of Focused Ion Beam and Scanning Electron Microscopy (FIB-SEM) was used to characterise the cross-section of the marker samples after W7-X plasma exposure and manual extraction from the stellarator vessel. A simulation model was developed to assess the uncertainty of the ps-LIBS method in depth owing to the surface roughness. Laser ablation rates of the different layers were determined by the profilometry and used to obtain *quantitative* erosion/deposition patterns of C and Mo. The heat load pattern of the TDU from the standard discharge of W7-X were adopted to compare with LIBS measurements for the erosion pattern. Finally, peak erosion amounts and rates of C which are representative for the whole vertical target of the uncooled graphite TDU in W7-X are obtained.

2. Measured sample and Experimental setup

2.1. Target elements: marker samples

TM2v2 target element, which consists of 5 individual marker graphite tiles (typically 75 × 55 × 30 mm^3 dimensions for one marker graphite tile), was analysed in the laboratory by the ps-LIBS method. TM2v2 target element was retrieved from the W7-X vessel after successful completion of OP1.2A. Fig. 1(a) shows a CAD drawing of TDU HM50 with the vertical divertor target element TM2v2 indicated. The green arrow in Fig. 1(a) indicates the ps-LIBS measurement direction on the target element. The full poloidal extension of the vertical target element TM2v2 from the Inner Wall (IW) or baffle region towards the divertor Pumping Gap (PG), located between the horizontal and the vertical target modules of the TDU, was scanned by ps-LIBS with a lateral resolution of 5 mm. The TM2v2 was exposed to 2481 seconds of H and He plasmas in standard magnetic divertor configuration in the campaign OP1.2A which corresponds to 65.7% of the total operational time of W7-X. Details of plasma operation and wall conditioning have been listed and summarised in our previous work [6]. Fig. 1(b) shows a photographic image of one of the 5 individual marker graphite tiles after plasma exposure and ps-LIBS analysis. The exact location of the photographed graphite tile rotated 90 degrees in clockwise direction is shown and indicated using the grey rectangle on the TM2v2 in the Fig. 1(c). The shaded grey area in Fig. 1(b) represents the C and Mo marker area on the graphite tile. The whitish dots with a diameter of 1 mm show the craters after the ps-LIBS measurement. Three typical scan lines of ps-LIBS with a line distance of 10 mm on the marker area were investigated. The top, centre and bottom scan lines of ps-LIBS are marked using green, red and blue circles to distinguish them.

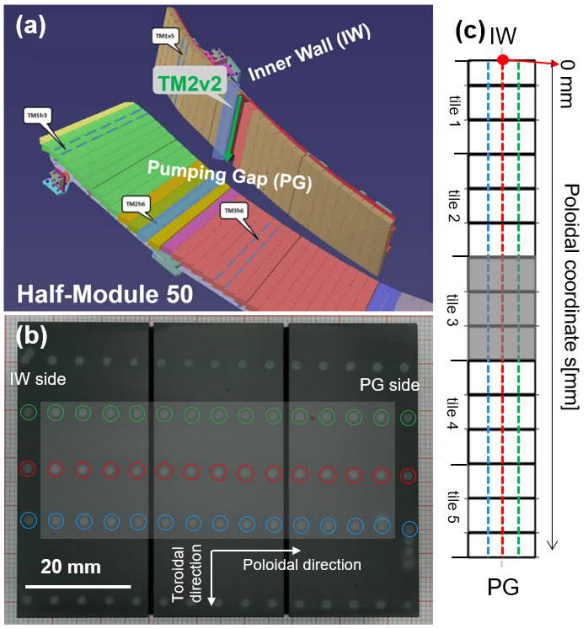

Fig. 1. (a) Schematic representation of the position of the TM2v2 vertical divertor target element located at TDU half module 50. IW is the direction towards the inner wall, PG is the direction towards the divertor pumping gap between the horizontal and the vertical target of the TDU. The arrow indicates the direction of ps-LIBS measurements along the TM2v2 target element. (c) The schematic and poloidal coordinate of TM2v2 vertical divertor target element. The origin of poloidal coordinate is marked by red dot. Three typical scan lines of

ps-LIBS on the marker area are marked using green, red and blue dotted lines. The line distance is about 10 mm. (b) Photo of one of 5 individual marker graphite tiles after W7-X plasma exposure and ps-LIBS analysis, the location of this photo is indicated by the grey area in the Fig. 1(c); the whitish dots represent the craters after ps-LIBS measurement. Some additional craters are visible outside the marker area.

Fig. 2 shows correspondingly a schematic diagram of the experimental set-up indicating the graphite sample and the arrangement of the ps-LIBS. The marker on the graphite target element tiles consists of a 0.2-0.4 µm thick layer of Mo and a 5-10 µm layer of C on top, which were deposited as a ~2 cm wide stripe in the center of the graphite tiles. The Mo inter layer represents a marker for distinguishing the C top layer and the graphite substrate of the TDU and permits the depth analysis (z direction in Fig. 2). The samples were scanned by the ps-laser with a lateral resolution of 5 mm - first crater 2 mm from left edge. The scanning direction of the ps-LIBS was in the poloidal direction from IW to PG. In order to assess the local erosion and deposition, every crater location, marked by the red dots, was ablated using minimum 200 laser pulses in order to ensure the removal of the whole marker layer and to obtain the material composition with depth resolution.

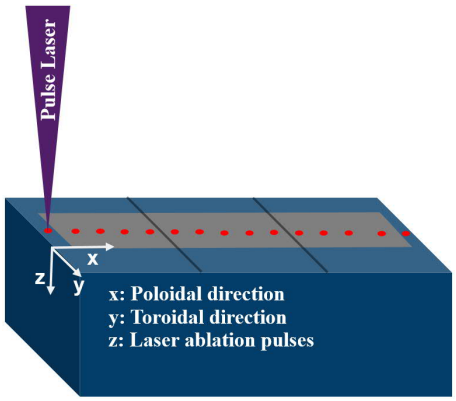

Fig. 2. Schematic diagram of the measured sample and the measurement design of ps-LIBS. X is the scanning direction of the ps-LIBS and also the poloidal direction in W7-X. Y is the toroidal direction in the W7-X coordinates. Z is the depth measurement direction associated with multiple laser pulse exposition.

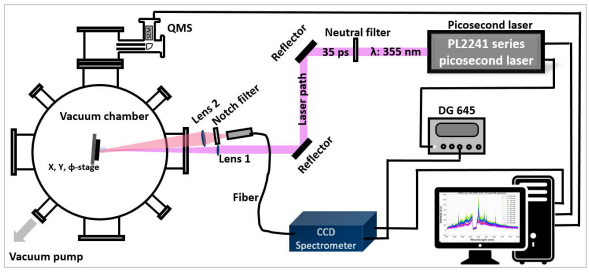

Fig. 3. Schematic of the ps-LIBS setup with vacuum chamber and sample, laser optics, fiber optics for the spectroscopic signal, and data acquisition.

2.2. Experimental setup

A schematic diagram of the ps-LIBS setup is shown in Fig. 3. A picosecond laser (EKSPLA, PL2241, wavelength: 355 nm, repetition rate: 10 Hz, pulse width: 35 ps) was employed to produce a laser-induced ablation plasma. The laser beam was focused by a plan-convex quartz lens with a 500-mm focal length on the measured sample. By focusing the laser beam and adjusting the laser amplification, a crater diameter of 1 mm and a pulse energy of 18 mJ at the sample were achieved. This resulted in a laser fluence of 2.3 J/cm^2 on the sample, which is a suitable fluence for the laser-based ablation techniques [21]. The sample was mounted on an X, Y, φ translation stage inside a vacuum chamber equipped with quartz windows. The vacuum chamber was pumped down to a pressure of 2×10^{-7} mbar. The laser beam hits the sample at normal incidence (90 ± 2°). The plasma emission plume was collected in a quasi-coaxial direction and guided by a lense (f=300 mm, d=100 mm) to a single-core optical fiber (Quartz, d=600 µm) into a 2048 pixels CCD spectrometer (HR2000 Ocean optics, 25 µm entrance slit, 600 grooves/mm). The compact spectrometer covers at once the wavelength span from 350 nm to 800 nm. The shortest integration time of the CCD is 1 millisecond. A multi-notch filter designed for wavelengths of 355 nm, 532 nm and 1064 nm with 50 mm diameter was placed before the fiber to block the scattered laser light and to protect the CCD detector. A digital delay generator (DG645) was employed to synchronize the picosecond laser pulses and spectrometer to obtain the spectra.

3. Discussion of the layered structure measured by LIBS

3.1. Depth-profiling of the target element TM2v2

Recorded spectra were processed as follows: (i) blank background spectrum subtraction, (ii) normalisation to avoid matrix effects and plasma fluctuations according to [22], and (iii) the average of three pixels around the maximum line intensity to omit jitter effects of the spectrometer [23]. Typical LIBS spectra in the wavelength span between 545 nm and 665 nm of target element tile (TM2v2) at different laser pulses for the same spatial location resulting in one crater are shown in Fig. 4. Emission lines of different atomic species like Mo, Na, H, C can be clearly identified. The spectral intensities of the observed lines vary, especially for the Mo atomic lines, from laser pulse to pulse and thus at different depths in the sample. Fig. 5 shows the emission intensities of C and Mo as function of the laser pulse number. The C emission is obtained as average of the C II lines at 426.73 nm and 657.80 nm, respectively. The Mo emission is determined by the average of Mo I at 550.67 nm, 553.30 nm and 557.04 nm. The use of averaged line intensities instead of single line intensities enhances the signal robustness and reduces relative standard deviations of the C and Mo emission, especially for laser pulses where the signal intensities are low. Note that the CII line at 657.80 nm might potentially interfere with a C I line nearby (657.88 nm), but that it has for this work no further impact on the interpretation.

Based on the emission features of the C and Mo in Fig. 5, three emission regimes as function of laser pulses could be identified. The transition interfaces of these three emission regimes are determined by the intersection of the Mo emission and the interface threshold (The interface threshold intensity was defined as the intensity of the Mo emission at the first C/Mo interface. The first C/Mo interface is determined utilising the linear correlation coefficient method which is the Pearson product-moment correlation coefficient described in [24, 25]). This method has the advantages of eliminating experimental noise, e.g. laser fluence fluctuations and pulse-to-pulse spectral fluctuations. A typical C/Mo interface determination utilising the linear correlation coefficient method is shown in Fig. 6. The depth profiles of the linear correlation coefficient corresponding to the spectra of the 3rd (C marker layer), the 90th (Mo marker layer) and the 295th (substrate graphite) ablation pulse are shown in Fig. 6(a). In general, 200 laser pulses are applied for the routine ps-LIBS measurement, but for the purpose of the substrate analysis also once 300 pulses were carried out to determine the ablation rate of the substrate (see section 5.2).

The depth profiles of the linear correlation coefficient and a 2D image of the linear correlation coefficient matrix between all the same spectra of this analysed crater are shown in Fig. 6(b) and (c), respectively. Note that the three typical spectra selected in Fig. 6(a) may not be universal for other analysed craters due to the differences of the layer thickness. Therefore, the depth profiles of the liner correlation coefficient between all the same spectra (e. g. Fig. 6(b)) should be plotted to cross-check with Fig. 6(a). Here, we suggest that it is best to use the same method as Fig. 6(b) to check the layer interface first, then select the representative spectra for the different layers to plot the linear correlation coefficient for displaying the interface clearly. This has the advantage of avoiding errors in the interface determination due to incorrect selection of representative spectra.

As shown in Fig. 5, the uncertainties in the determination of the interfaces from the first regime to the second and from the second to the third regime due to the fluctuations of the recorded spectral signal are 3 laser pulses and 20 laser pulses, respectively. These fluctuations are mainly caused by the relatively low laser fluence used in order to obtain a high depth resolution, associated with lower ablation volume, on cost of corresponding light emission from the ablated species. Indeed, the interface threshold of the Mo emission determined by the linear correlation coefficient was very close to the 3 times the standard deviation of the background intensity near the Mo I lines in our previous work [17]. Based on Fig. 5, in the first regime, which lasts for about the initial 55 laser pulses, C emission was clearly recorded spectroscopically, while Mo emission was very weak and noisy, or even was not detectable at all. The observed C emission in this case is caused by the ablation of the C layer on top of the target element. The ablated surface layer in this first regime is therefore labelled in the following as C emission layer. The second regime, associated with Mo emission, is observed with increasing number of laser pulses. Thereby, the Mo emission appears quickly and then drops slowly until it disappears at about the 190th laser pulse. Noticeably, the C emission can be recorded uninterruptedly in this second ablation regime. Based on the co-appearance of Mo and C emission, the ablated layer in the second regime is labelled in the following as the Mo-C emission layer. With consecutive laser pulses, the laser ablates the substrate graphite and the third regime can be identified. In this regime, the C emission tends to be stable and the Mo emission fades away as the Mo marker layer is completely removed. Thus, the third regime is called in the following the substrate graphite.

It is remarkable, that the C emission can always be observed in the LIBS spectra, even during the phase where the laser ablates the Mo marker layer of the sample. Moreover, the number of pulses of the Mo emission in the spectrum greatly exceeds the expectations from our a priori information in which the Mo emission signal maybe only observed in about 10-20 laser pulses due to the fact that the deposited Mo marker layer thickness is only 0.2-0.4 µm [6] and the ablation rate of pure Mo bulk is about 24 nm [21, 26]. Different layer determination methods for the LIBS technique, the cross-section of the normalised intensities method [27, 28], the cross-section of the emission intensity ratio method [29, 30], were also investigated to reduce the observed Mo emission tail and to sharpen the interfaces between the three regimes. However, the results determined by these two layer determination methods were close to the results determined in Fig. 6, especially for the cross-section of the emission intensity ratio method. These two methods therefore also cannot obtain the sharp interfaces. Thus, we have to consider that there are several potential asymmetry factors which avoid a perfect layer-by-layer ablation process resulting in (i) a long-lasting Mo emission with a tail and (ii) continuous C emission in the second regime. The possible reasons for the potential asymmetry factors are investigated in the next two section (3.2 and 3.3).

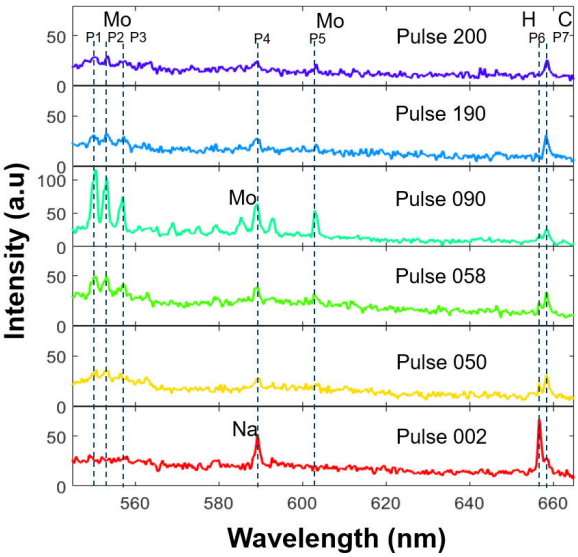

Fig. 4. Typical LIBS emission spectra of the vertical target element with marker layer for different laser pulses after blank spectrum subtraction. P1-P3 and P5 indicate the Mo I emission at 550.67 nm,

553.30 nm, 557.04 nm, and 603.06 nm; P4 indicates the spectrally unresolved line emission of Na I at 588.99 nm and 589.59 nm in the 2nd pulse; P6 indicates the H I emission at 656.27 nm, and P7 indicates the C II at 657.80 nm.

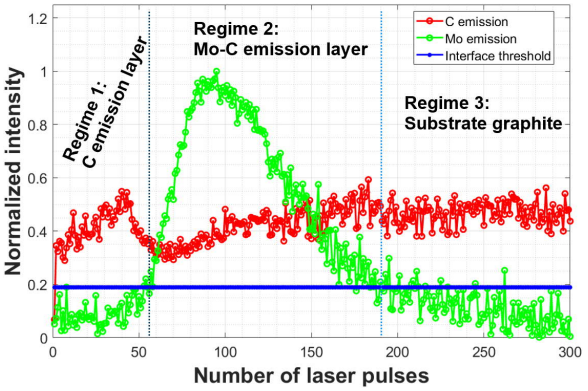

Fig. 5. C and Mo emission as function of laser pulse number. Three emission regimes can clearly be identified and assigned as C emission layer, Mo-C emission layer, and substrate graphite.

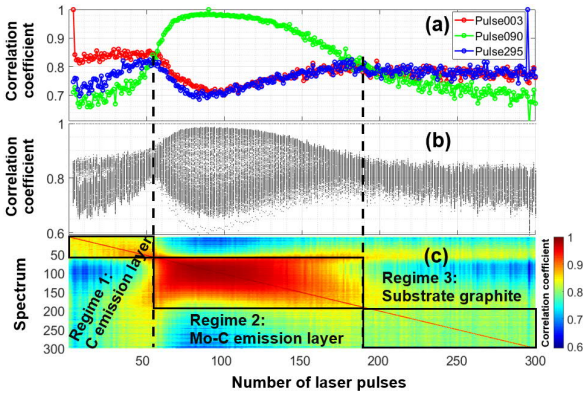

Fig. 6. Correlation coefficient obtained from the same spectra sequence as used in Fig. 5. (a) The depth profiles of the correlation coefficient corresponding to spectra 3rd (C marker layer), 90th (Mo marker layer) and 295th (substrate graphite). (b) The depth profiles of the linear correlation coefficient between all the recorded spectra in one analysed crater. (c) 2D image of the linear correlation coefficient matrix.

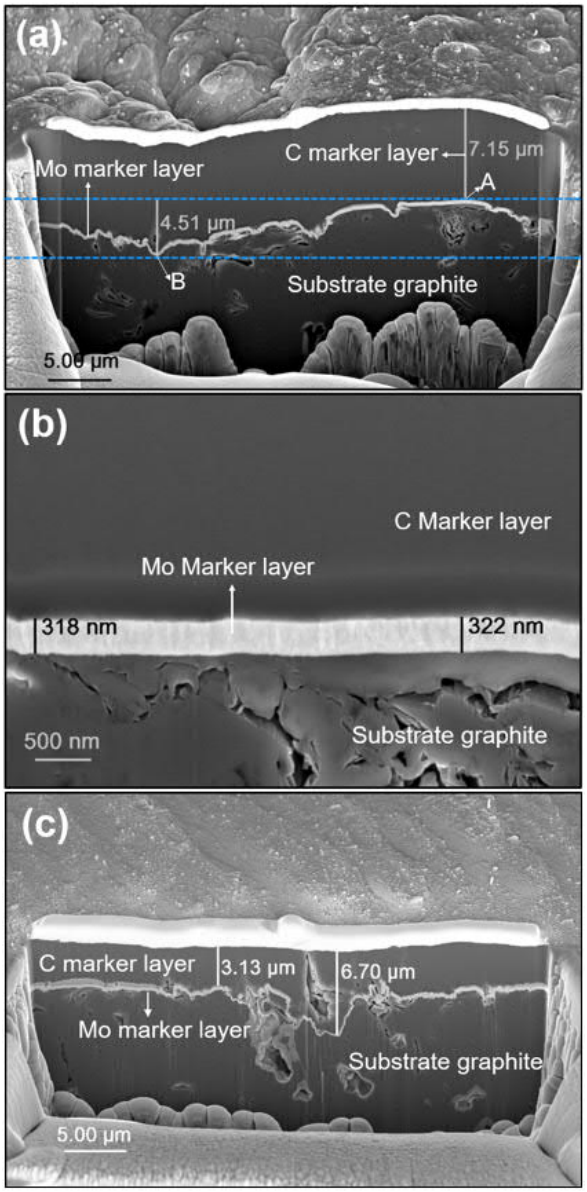

Fig. 7. (a) Cross-section of the marker layer on top of the target element TM2v2 in the poloidal location with low hydrogen plasma fluence (little plasma contact zone). The marker layer structure is intact with the top C layer thickness of about 7.15 µm, the layer region with Mo appearance marked by the two blue dotted lines with a thickness of 4.51 µm reflecting the large surface roughness of the graphite substructure in this 45 µm wide SEM figure. (b) Close-up view of the cross-section of Fig. 7(a) visualising the pure Mo interlayer with a thickness of about 0.32 µm deposited above the porous bulk graphite substrate. (c) Cross-section of the marker layer of the target element TM2v2 in the poloidal location with high hydrogen plasma fluence (erosion zone). The top C layer was eroded and the surface roughness was reduced due to W7-X plasma impact.

3.2. Potential asymmetry factors on depth analysis due to layered material structure

Combined Focused Ion Beam (FIB) cutting and Scanning Electron Microscopy (SEM) imaging was applied to

characterize the cross-sections of the little plasma contact zone and the erosion zone on the vertical target element after W7-X plasma exposure. The results are shown in Fig. 7. Three areas can clearly be distinguished and identified in the SEM image (Fig. 7(a)): the C marker layer on top, the pure Mo marker layer in the middle, and the substrate graphite at the bottom. The C marker layer thickness at this FIB-SEM measurement location is about 7.15 µm (Fig. 7(a)) whereas the pure Mo marker layer thickness amounts to 0.32 µm (Fig. 7(b)). This FIB-SEM cross-section confirms the initially deposited layer structure from the CMSII manufacturing process with a 5-10 µm thick C top layer and a 0.2-0.4 µm thick marker layer made of Mo [3, 5, 6]. At little plasma contact zone, the pure Mo layer follows the morphology of the graphite substrate surface with its roughness in the few µm scale. In the 45 µm wide measurement window of the SEM image shown in Fig. 7(a), the region with Mo content extends up to 4.51 µm in depth, as indicated by the two blue dotted lines, though the real thickness of the pure Mo interlayer amounts less than a tenth of this apparent extension. At the erosion zone, the pure Mo layer follows the morphology of the graphite substrate surface, but the top C layer was eroded by the W7-X plasma which reduces the surface roughness comparing with the little plasma contact zone shown in Fig. 7(a). The lateral dimension of the laser spot (diameter) during the ps-ablation process is more than a factor 20 larger than the spatial extension of the shown SEM image (Fig. 7(a) and 7(c)). Thus, in the LIBS measurement, the Mo line emission in the ps-LIBS spectrum could be detected within this Mo-containing region up to 4.51 µm thickness where the 0.32 µm Mo interlayer on the rough graphite substrate surface is present. The laser e.g. could first ablate the Mo at the shallow position A and subsequently Mo from the lower position B depicted in Fig. 7(a). The appearance of the emitted Mo emission rises then gradually at the beginning and decays slowly with further laser ablation repetition. Moreover, the C emission shall be always detectable in the LIBS spectrum as C results from both the top C layer as well as the graphite substrate. Indeed this behavior of Mo and C emission can be seen in the previously discussed Fig. 5. The morphology of the graphite substrate, on which the thin Mo interlayer is deposited, is one of the potential reasons explaining the width and asymmetry of the measured Mo emission, thus also the long tail in Mo with rising laser pulse number. For the erosion-dominated areas in the target element, e. g. one shown in Fig. 7(c), this effect is much more pronounced because the surface morphology is considerably smoother than the initial marker coated target element. Note that, the appearance of the long tail might also be further enhanced by deposition of some Mo during the CMSII process in cavities embedded in the porous graphite substrate [6].

3.3. Potential influence of the applied laser beam on the layered material analysis

Apart from the properties of the marker layer structure of the sample itself, also the laser beam properties of the applied ps-LIBS system can contribute to the observed long Mo emission tail. The optimum laser beam for a ps-LIBS analysis system would be a perfect rectangular (or flat-top) beam without any internal substructures due to power fluctuations. Fig. 8 shows the 2D beam profile analysis for the actually applied laser system and the cross-section of the beam center measured by an area array laser beam analyser. A nearly circular output beam (major axis: 13.14 mm, minor axis: 13.01 mm) is observed by the beam analyser. The diameter of the applied laser beam is about 13 mm at the laser output. The measured laser beam is neither a pure Gaussian beam nor a pure flat-top beam, but rather a combination of both – a flat-top-like beam. Note, the vertical dark line in the Fig. 8(a) is due to a damaged pixel array in the laser beam analyser.

Owing to the imperfect flat-top-like laser beam profile and the resulting non-rectangular cross-section of the ablated crater, the Mo emission does not change abruptly when the bottom of the ablated crater reaches a Mo/C-layer interface like e.g. at position B in Fig. 7(a). At the edge of the laser beam, where less power for ablation reaches the sample, still remains of the Mo interlayer can exist at the edge of the non-rectangular cross-section of the ablated crater; the edge will be ablated in subsequent laser pulses and result in Mo line emission. This phenomenon was much obvious when the Gaussian beam was adopted [31]. The energy distribution of the laser beam measured by the analyser is shown in Fig. 8(b). This cross section of the laser beam is extracted from the horizontal line marked in yellow in Fig.8 (a). More examples of laser beam analysis of the present system can be found in [32]. The energy distribution is not perfectly smooth at the beam center and small fluctuations of up to 20 % exist. These energy fluctuations of the laser beam are sufficient to induce some roughness at the bottom of the crater centre during the ablation process. Depending on the combination of fluctuation amplitude, layer thickness, and ablation rate of the involved layer materials, a smearing of the transition between the two layers might be induced. In the present case, the imperfect laser energy distribution property could contribute to the observed tail in Mo emission in addition to the previously described non-rectangular laser beam profile.

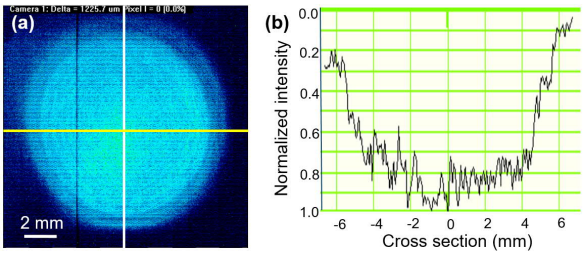

Fig. 8. Laser beam profile of emitting wavelength of 355nm at the distance of 32 cm measured by an area array laser beam analyzer. (a) The 2D laser beam topology is shown in the left figure, a nearly circular output beam is observed. The diameter of the laser beam is about 13 mm. (b) The cross section of the energy distribution along the horizontal line of the laser beam marked in yellow.

4. Principle simulation model of multi-pulses laser ablation

As was discussed in the previous sections 3.2 and 3.3, both laser beam profile and the surface roughness of the Mo layer

determine the shape of the ps-LIBS produced Mo emission distribution. These effects result in the depth analysis by ps-LIBS in more laser pulses with detectable Mo emission in comparison with the number of ablation pulses in bulk Mo which is done in reference experiments [21, 26]. Thereby, a simulation model was developed and employed to investigate the measurement uncertainty caused by the laser beam effect. The model is based on the surface morphology module, which was implemented into the 3D Monte-Carlo code ERO2.0 and validated in multiple experiments [33]. In the model a perfect flat-top laser beam was assumed and used to ablate the target with multi-layer structure used in W7-X as described in section 2.1.

A schematic diagram of the layered sample in the simulation model is shown in Fig. 9. The dark grey part, blue part and light grey part represent the substrate graphite, Mo marker layer and C marker layer in the layered sample, respectively. The cavities in the substrate were ignored. One should note that this is only a schematic diagram, the shapes of the Mo marker layer in Fig. 9 do not represent the real shapes of the Mo marker layer in graphite tiles. A typical 3D surface morphology of a small, but representative subarea (40 μm x 40 μm) of the target element graphite tile after OP1.2A campaign is depicted in the inset of Fig. 9. In order to estimate the effect of the surface roughness of the C substrate and the Mo layer on the observed signal, various assumption concerning this roughness have been tested according to the represented roughness in the FIB-SEM measurements. Additionally, the surface roughness of the top C marker layer after OP1.2A campaign plasma impact was taken into account in the simulation and assumed to be 1 μm, e. g. the inset of Fig. 9. Such surface has been used in the model as target surface on which the ablation process through the three layers was simulated. Indeed, this used roughness in the model is comparable to the surface roughness at the massive erosion zone.

One should note, that the area of the laser beam was larger than the area considered in the simulation model (the laser beam on the target is 1000 μm, while the length of the patterns of the Mo marker layer is 40 μm in the model which is 25 times less than the diameter of laser beam on target). This means that the observed emission signal is the result of ablation in different points which cannot be reliably represented with one analytical formula. Totally 24 different shapes of the Mo marker layer described by the combination of sinusoidal and linear functions were assumed to following the substrate graphite surface in the model in order to represent the real surface of the target element graphite tile as good as possible. Some examples of these shapes of the Mo marker layer and substrate graphite surfaces are shown in Fig. 10. The thickness of the Mo marker layer was 0.32 μm, a typical value as determined by FIB-SEM e. g. Fig. 7(b). The profile of the Mo interlayer was shaped based on the set of recorded FIB-SEM images which include the two shown in Fig. 7(a) and 7(c). One should note that the FIB cut (Fig. 7(a)) is only used to show the potential shape of Mo interlayer in the model and not used to show the surface roughness after high plasma impact. Indeed, the plasma has done multiple erosion and deposition processes under shallow angle impact which causes smearing and in this case reduces the surface roughness, like the case shown in Fig. 7(c). In the model, the surface of the top marker layer after the plasma impact in OP1.2A was assumed to be the inset in Fig. 9. The shapes of the Mo marker layer was mainly defined by an analytical formula which is the combination of sinusoidal and linear functions, just like the Fourier transform. Moreover, three different ablation rates according to the three different layers were applied: 108 nm/pulse for the C marker layer, 24 nm/pulse for the Mo marker layer, and 30 nm/pulse for the graphite substrate. The values were taken from previous as well as new studies presented here [26].

A comparison between the modeling results and experimental results is shown in Fig. 11. The blue and red solid lines describe the experimental results obtained for Mo and C partial abundances. The black dotted lines represent the set of modeling results for the individual shape patterns of the Mo marker layer and the graphite substrate surface studied (like in Fig. 10). The blue and red dotted lines show the modelled Mo and C partial abundance obtained by a combining the simulation results of the 24 different shape patterns of the Mo marker layer and the graphite substrate surface together. The manifold of 24 different roughness shapes with various amplitudes, frequencies, phases of the analytical formula shall demonstrate the impact of potential variations within the observed pattern structures close to the random 3D structure observed from FIB-SEM. This number of shapes was based on the trade-off between the computational time used for simulations and sensitivity of the final result for adding new shapes. When combining simulation results with various topography shapes, same shapes could have been repeated more than ones in most of the areas. However, for areas experiencing high re-deposition values, different values of C/Mo thickness might need to be considered in the model in future.

As the results shown in Fig. 11, C partial abundances and Mo partial abundances in the model results at the left side of the grey area are in agreement with experimental results. However, for both Mo and C covered by grey area, modeling results show a faster decline with the amount of pulses than in the experiment. A possible reason for this disagreement is the fact that a perfect flat-top laser beam was assumed in the model, while a flat-top like laser beam with the described energy fluctuations was employed in the ps-LIBS experiment. Here, e.g. at the edge of the flat-top like laser beam, where less laser energy for ablation reaches the sample, could continue to ablate the Mo marker layer and C marker layer at the outer edge of the non-rectangular cross-section of the ablated crater. This effect could slow down the decline of the Mo and C signal which are indicated by the grey area in the Fig. 11. Therefore, the gap between modeling and experiment marked by the grey area in Fig. 11 could be considered as the measurement error from the redundant ablation of the target caused by the flat-top like laser beam. By integrating the area under the modeling curve and the experimental curve, the gap area between model and experiment is calculated to 35% of the experimental curve area. Thus, the imperfect shape of the laser beam could

increase the measurement value for the Mo-C emission layer by 35%, which should be considered and corrected in the quantification of the depth-profiling of the vertical target element TM2v2 installed in the TDU.

As shown in Fig. 11 and discussed above, the gap area between model and experiment are mainly caused by the long Mo tail or the falling edge of Mo. On the rising edge of Mo, the modeling and experimental results are matched very well. In the LIBS quantitative analysis, at the locations where the C marker was not completely eroded during the OP1.2A, the quantification of the erosion or deposition at these locations is determined using the raising edge of Mo or in other words: the first Mo/C interface (e. g the first interface of Mo/C in Fig. 5). In this case, ps-LIBS results do not require correction utilising the modeling result. In this work, these locations are generally located at the little plasma contact zone on the target element TM2v2 which is discussed in detail at section 5. On the contrary, at the massive erosion zone where the entire C marker layer was eroded in OP1.2A, the surface roughness was reduced by the W7-X plasma. The quantification of ps-LIBS can be corrected utilising the principle modeling results; the long Mo tail or falling edge of Mo is adopted in the estimation of erosion.

Note, that the presented model is the first attempt to address the impact of Mo layer surface roughness in the ps-LIBS interpretation. It is presented to demonstrate the general approach. The present model is capable of explaining the shape of the Mo signal curve, however, it cannot provide a precise estimate of the Mo layer roughness. More detailed studies and a further development of the model is planned in the future.

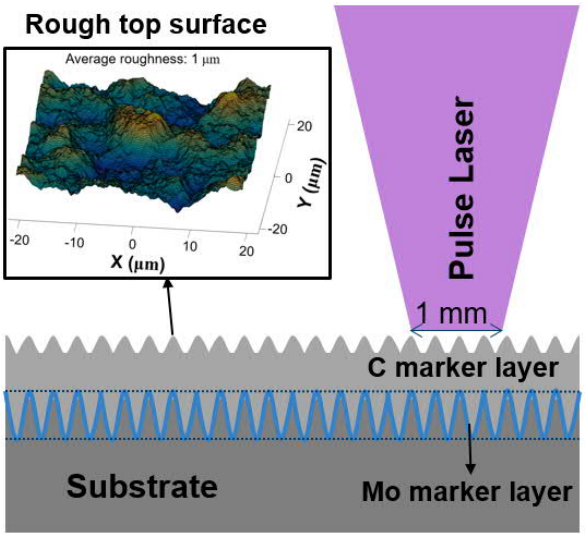

Fig. 9. Schematic representation of the layered sample in the simulation model. The dark grey part, blue part and light grey part represent the substrate graphite, Mo marker layer and C marker layer of the layered sample in the model, respectively. An inset in the figure represents a typical top 3D surface morphology of the layered sample applied in the model. The surface structure of the inset is derived from several FIB-cuts recoded with SEM of studied target element TV2v2 prior to ps-LIBS exposure.

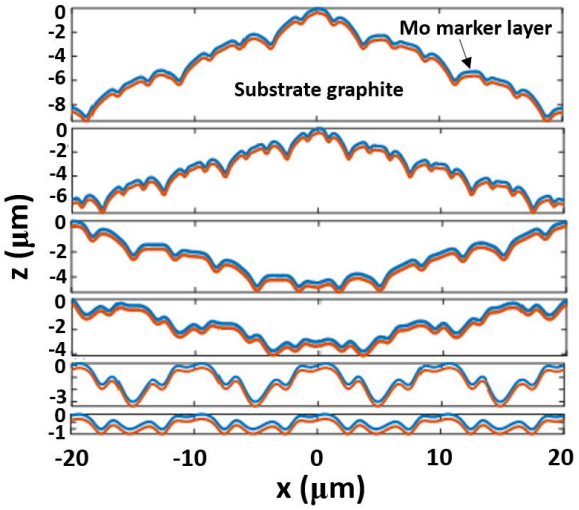

Fig. 10. Typical 6 different shapes of the Mo marker layer and the substrate graphite surface employed in the model. The assembling of the shapes described by the combination of sinusoidal and linear functions were employed to simulate real Mo marker layer shown by the FIB-SEM images prior to ps-LIBS exposure as good as possible. The blue part show the Mo marker layer. Above and below the blue part represent the C maker layer and substrate graphite, respectively.

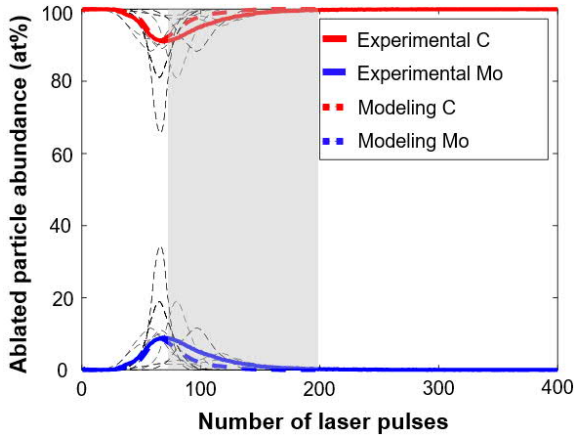

Fig. 11. Comparison of the modelled and measured C and Mo ablation particle abundance as function of applied ps-LIBS pulses. The black dotted lines represent the variety of modeling results for different shapes of Mo marker layer and graphite substrate surface. The blue, red dotted lines reflect the combination of 24 different surface shapes modelled. The gap marked by grey area between the model and experimental results is calculated to 35% of the experimental curve area.

5. Ps-LIBS measurements on the target element TM2v2

5. 1 Qualitative analysis of the erosion/deposition pattern

As described in section 3.1, the erosion or deposition of the target element surface can be qualitatively correlated with the Mo emission during the depth profiling with increasing number of ablating laser pulses at the same spatial location. Fig. 12(b) shows the heat load pattern of a representative W7-X discharge in the very same standard magnetic configuration recorded with IR thermography. For this typical discharge in

standard configuration, the planar coil correction current was |-700 A| and the plasma-induced toroidal current reached 2kA. Fig. 12(c) represents the depth profile of H I 656.27 nm at the centre scan line of ps-LIBS along the poloidal direction. The H pattern in the poloidal direction matches well with the IR thermography image in which the erosion-dominated area shows a lower fuel emission intensity and lower fuel retention depth. Fig. 12(d)-(f) show the depth profile of Mo emission at the three scan lines of ps-LIBS along the poloidal coordinate of the vertical target element TM2v2 from the IW to the PG. The data is hereby discretized with 72 measurement points over the about 355 mm length of the TM2Vv2 target element. Each measurement point with about 1 mm diameter is separated by 5 mm with respect to the next spot with about 1 mm diameter. The experimental data points are then interpolated in the visulisation resulting in a continuous emission along the poloidal coordinate. Three scan lines with the line distance of 10 mm were indicated in the schematic of TM2V2 in Fig. 12(a). Moreover, the three scan lines on the one of the 5 individual marker graphite tiles are also indicated and marked using green, red and blue circles, which can be found in the Fig. 1(b). In this work, IW is the direction towards the baffle / inner wall, PG is the direction towards the pumping gap between the horizontal and the vertical target elements of the TDU. The zero point of the poloidal coordinate in the Fig. 12 was defined by the start of the vertical target element TM2v2 at IW as also shown in Fig. 1(c).

From the Fig. 12(d)-(f) results, a similar erosion/deposition pattern was observed in the toroidal direction within 20 mm indicated in the Fig. 1(b) on the marker area of vertical target element TM2v2. In the poloidal direction, a massive erosion zone can clearly be identified between the poloidal positions s=125 mm and s=225 mm because Mo emission can be recorded already in the very first ablation pulse of the depth analysis scan. Thus, the entire C marker layer of several µm thickness initially deposited above the Mo marker layer was completely eroded during W7-X plasma operation in OP1.2A campaign. The peak erosion is located around the poloidal position s=175 mm which reflects the strike-line position on the vertical target in the dominant magnetic divertor configuration in OP1.2A.

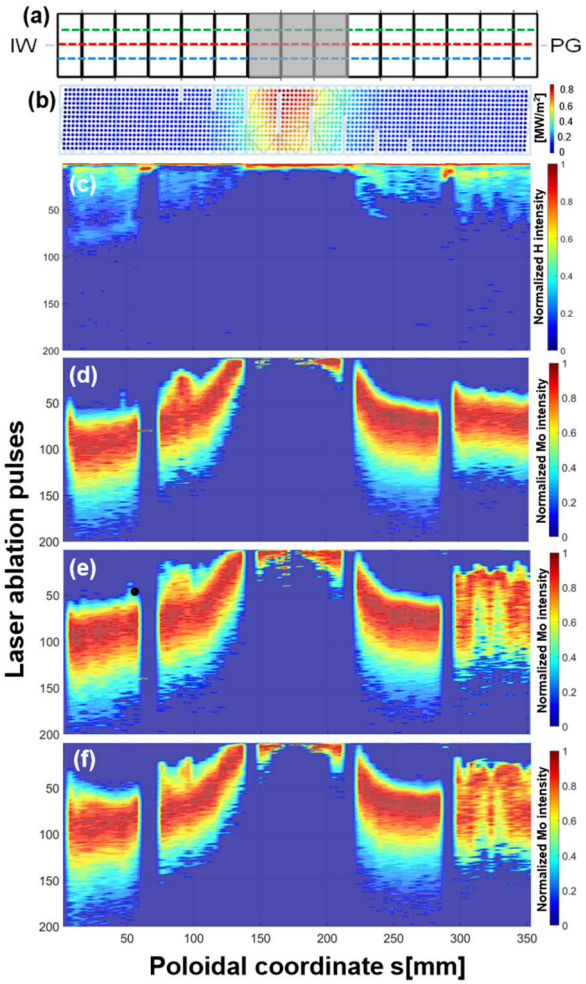

Fig. 12. (a) The schematic of the TM2v2 target module from IW to PG. (b) Representative IR thermography image of the heat load at the vertical target position of the analysed tile. (c) Depth profile of Hα in the poloidal direction for the centre scan line of ps-LIBS, the corresponding Mo emission at same location is shown in (e). Depth profile of the Mo line emission in poloidal direction for the top (d), centre (e) and bottom (f) scan lines, indicated by green, red and blue dotted lines in Fig. 12(a). The grey area in Fig. 12(a) represents the location of the graphite tile shown in Fig. 1(b). The origin of the poloidal coordinate (s=0 mm) is defined as the very top of the IW side and also can be found in Fig. 1(c). The small black solid dot in Fig. 12(e) shows the zero erosion and deposition position.

As the comparison between LIBS results and heat load pattern recorded by IR thermography image in Fig. 12, the strike-line, thus the location of highest impinging heat, the particle load of plasma and impurity ions correlate with the erosion pattern on the analysed target element measured by ps-LIBS. Moreover, the IR image proves that a higher particle flux results in a higher temperature and higher erosion, simultaneously. This implies that the high temperature caused by the particle flux during plasma operation was sufficiently high that trapped fuel in the target was desorbed. The combination of high temperature and high erosion could lead to the low fuel content and low fuel retention depth at a higher particle flux location. Furthermore, at the peak erosion

locations, the Mo emission could only be recorded in the first three laser pulses and subsequently vanished. Thus, the erosion by physical sputtering during plasma operation in W7-X was so strong, that also the Mo marker layer was almost completely eroded. Considering the role of the surface roughness of the substrate mentioned before, one might conclude that the residual Mo was likely just located in valleys of the rough surface and the majority of the Mo layer was just completely removed. The sputtering of Mo can under typical divertor conditions in W7-X only occur by impurity ions like oxygen and carbon. This conclusion is in line with a recent analysis of the impurity content of these W7-X plasmas with about 7% of O in the edge layer [34] prior to boronisations [7].

5.2. Laser ablation rates of different layers

To quantify the absolute erosion/deposition pattern by ps-LIBS, the laser ablation rates of the different layers including the C emission layer, Mo-C emission layer and substrate graphite need to be known or experimentally determined. Ten different craters were ablated by using different laser spots on the target element TM2v2 around the almost pristine region between s=10 and s=57 mm in Fig. 12. Subsequently, the crater depth analysis was carried out by surface profilometry. The selection criterion for the relative pristine marker areas and these various laser pulses for the ten craters are based on the depth-profiling of the Mo emission in the Fig. 12(d)-(f). A large number of laser pulses was applied to produce these ten craters and to derive the ablation rates of the C emission layer (40, 58 and 60 laser pulses), the Mo-C emission layer (58, 60, 90, 120, 150 and 190 laser pulses) and the substrate graphite (190, 200, 250 and 300 laser pulses). A Dektak 6M Stylus profilometer was used to measure the ablation depth of these craters for different numbers of ablation laser pulses. The combination of both information and reference FIB-SEM cuts provides characteristic ablation rates for the different layers of the target element. A typical crater characterized by profilometery at the marker location and 200 laser-induced ablation pulses is shown in Fig. 13. The ablation depth is determined to be about 12.4 µm with an uncertainty of about 10% given by the relative standard deviation of the ablated crater depth. By linear regression the ablation depths of these craters produced by different laser pulses mentioned above, the Average Ablation Rates (AARs) of the C emission layer, the Mo-C emission layer and the substrate graphite are determined as 108±0.5 nm/pulse, 44±2.8 nm/pulse, and 30±3.8 nm/pulse, respectively. The results are shown in Fig. 14. The uncertainties of these AARs are the slope error obtained by the linear regression fitting for the measured data points. Note, that the AAR of the marker C layer is higher than the AAR of the substrate graphite which might be caused by micro-structures, optical properties and the incubation effect in multi-pulse laser ablation.

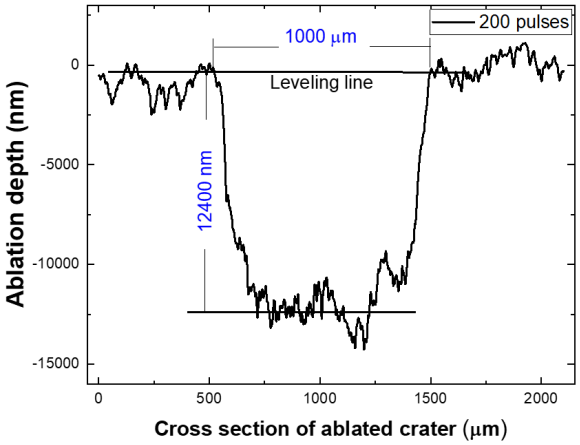

Fig. 13. Cross section of an ablated crater after 200 laser pulses at one spatial position on TM2v2. The diameter of the crater is about 1 mm, the total ablation depth is 12.4 µm and covers all three layers. The measurement uncertainty of this depth determination was estimated to be less than 10%.

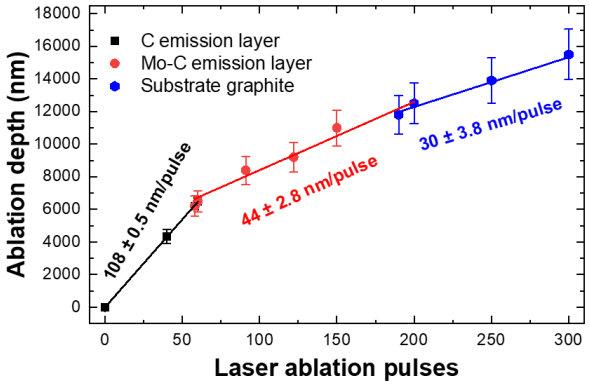

Fig. 14. Ablation depths produced by various laser ablation pulses at the relative pristine marker area on the target element TM2v2. Data points were measured by profilometry and solid lines were obtained by liner regression using the data points.

5.3. Quantitative analysis of erosion/deposition patterns

Material erosion and deposition on the divertor was investigated using the elastic backscattering spectrometry (EBS) technique via the measurement of the C and Mo amounts on the TDU tiles before and after W7-X plasma exposure in the OP1.2A campaign [6]. The EBS results showed that only very little depositions of C and Mo was observed in remote areas of the divertor due to little plasma contact. In this work, based on the EBS results for the same target element TM2v2 before and after OP1.2A, the changes of the C marker layer and Mo marker layer at the position s=57 mm of Fig. 12(e) are negligible. Therefore, we define this position indicated by a small black solid dot in Fig. 12(e) as the zero erosion and deposition position. At this position, both the material erosion and deposition are zero. In the ps-LIBS measurement, when the laser pulse numbers for removing the carbon emission layer at the measured position are greater than the laser pulse numbers for removing the C emission layer at this zero position, this measured position is identified as the

material deposition. Conversely, the measured position is identified as material erosion. By combining with the ablation rates of the different layers measured in section 5.2, for the first time, the absolute erosion/deposition amount patterns of C and Mo for the centre scan line (Fig. 12(e)) at the vertical target element TM2v2 in OP1.2A were mapped in Fig. 15 by ps-LIBS technique. In these calculations, the used densities of C and Mo are 1.8 g/cm^3 [35, 36] and 10.28 g/cm^3, respectively. The error bars in Fig. 15 are caused by the uncertainties in determination of the interfaces from the C emission regime to the Mo-C emission region and from the Mo-C emission regime to the substrate graphite regime, which regimes have been shown in Fig. 5. Here in the Fig. 15, the initial differences of the C marker layer and Mo marker layer on different positions of TM2v2, have been corrected according to the EBS results for the same element target TM2v2 before OP1.2A campaign.

As shown in Fig. 15(a), only very little deposition of C and Mo are observed from s=2 mm to about s=52 mm in the poloidal direction in remote areas due to the little plasma impact. A relatively wide net erosion zone with a poloidal extension from s=75 mm to s=270 mm was observed. This could be correlated to the main particle interaction zone at the magnetic strike-line of the dominantly applied standard magnetic divertor configuration and the movement of the strike line by toroidal currents [37]. As shown in Fig. 15(a) and (b), a massive erosion zone can be identified from 125 mm to 225 mm in the poloidal direction. In the massive erosion zone, the entire C marker layer deposited above the Mo marker layer was eroded by the W7-X plasma in OP1.2A. Noticeably, at the peak erosion position (s=175 mm) in the massive erosion zone, not only the entire C marker layer but also almost the entire Mo marker layer were eroded owning to a fact that the Mo emission can be observed only in the first three laser pulses. At the peak erosion position, not only 7.6×10^{19} C atoms/cm^2 but also 2×10^{18} Mo atoms/cm^2 were eroded due to plasma fuel particle (H, He) and impurity (O, C) ion impact in OP1.2A. These values are calculated assuming that a 100 nm thick C layer corresponds to 0.9×10^{18} C atoms/cm^2 (C density: 1.8 g/cm^3) and that a 100 nm Mo layer is equivalent to 0.65×10^{18} Mo atoms/cm^2 (Mo density: 10.28 g/cm^3). When taking the extrapolation relationship from the Mo erosion to C erosion in ref [6], the C erosion in the massive erosion zone could be extrapolated based on the eroded Mo data and the results are shown in Fig. 16. The extrapolated C erosion amounts up to 15×10^{19} C atoms/cm^2 at the peak erosion location. This amount of eroded C corresponds to a C layer with 16.67 μm thickness. A peak C erosion rate of 6.7±1.0 nm/s at the vertical target element of the graphite TDU can be derived for the 2481 plasma seconds in standard magnetic divertor configuration in the OP1.2A. The uncertainty of erosion rate is determined by the uncertainty of C erosion extrapolation shown by green line in Fig. 16. Moreover, the heat load obtained using the same data as the Fig. 12(b) is shown by the red line in Fig. 16. The erosion amount of C qualitatively matches with the heat load by the discharge in the standard configuration of W7-X.

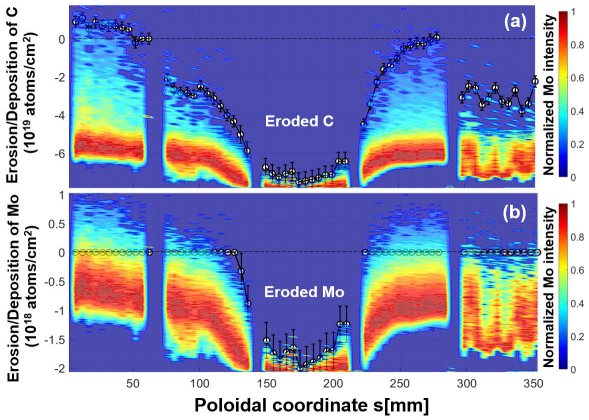

Fig. 15. The erosion amounts of C (a) and Mo (b) of the target element TM2v2 in OP 1.2A campaign for the centre scan line of ps-LIBS. Deposition has positive value and erosion has the negative sign. The exact location of this scan line is indicated by red dotted line in the Fig. 12(a), the same Mo emission data was used for Fig. 12(e).

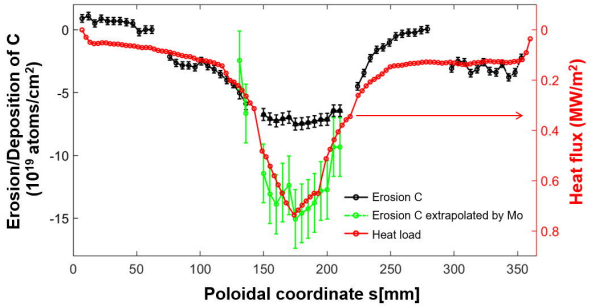

Fig. 16. Erosion/deposition amounts of C during OP 1.2A based on ps-LIBS technique. Deposition has positive value and erosion has the negative sign. Black line: measured data; green line: extrapolated erosion of C based on the erosion of Mo; red line: heat load at the standard discharge of W7-X in OP1.2A.

6. Conclusion

The materials erosion and deposition of C and Mo from the TDU tiles of W7-X was determined using the dedicated PWI target elements with C and Mo marker layers during OP 1.2A. A dedicated target element TM2v2 installed in the vertical divertor target element of Half-Module 50, was investigated by ps-LIBS technique in order to determine the local erosion/deposition pattern caused by W7-X plasma impact. The samples were scanned by the ps-laser with a lateral resolution of 5 mm in poloidal direction. Moreover, three typical scan lines of ps-LIBS with the line distance of 10 mm also were performed to investigate the toroidal variation within the range of 20 mm. The general erosion/deposition pattern on the target element was determined by depth-profiling of the Mo marker interlayer. Several potential asymmetry factors from the analysed sample and applied laser system, which avoid a perfect layer-by-layer ablation process and result in a C-Mo emission layer in the ps-LIBS technique, were proposed and discussed. A simulation model was developed to correct the LIBS results at the massive erosion zone with a value of 35% caused by the imperfect spatial profile of the applied laser

beam. The laser ablation rates of the different layers and the graphite substrate was measured utilising profilometry and cross comparison was made with FIB-SEM measurements. Thereby, for the first time, the net erosion/deposition pattern on the vertical target was mapped quantitatively by the ps-LIBS technique. The erosion patterns matched qualitatively well with the IR thermography image of a standard discharge of W7-X. A similar erosion/deposition pattern on the vertical target was observed in the toroidal direction within the range of 20 mm. A relatively wide net erosion zone in poloidal direction was extended by about 200 mm and can be correlated to the main particle interaction zone at the magnetic strike-line of the dominantly applied magnetic standard divertor configuration. A massive erosion zone can be identified extending by about 100 mm in the poloidal direction, where the entire C marker layer deposited above the Mo marker layer was eroded by the W7-X plasma in OP1.2A. The peak erosion position (s=175 mm) was observed in the massive erosion zone, where not only the entire C marker layer but also almost the entire Mo marker layer were eroded. At the peak erosion position, not only 7.6×10^{19} C atoms/cm^2 but also 2×10^{18} Mo atoms/cm^2 were eroded due to plasma fuel particle (H, He) and impurity (O, C) ion impact in OP1.2A. The extrapolated C erosion from Mo erosion is up to 15×10^{19} atoms/cm^2 at the peak erosion location. These amounts of the eroded C can correlate to a high peak C erosion rate of 6.7±1.0 nm/s at the vertical target element of the graphite TDU in the OP prior to boronisation.

The presented experimental results show that LIBS can be used to investigate the erosion/deposition of the PFCs, which is of great interest to study the PWI in W7-X for further operational phases. Moreover, due to the potential on-line diagnostic ability of the LIBS technique, the presented results also could provide a data support and exert a tremendous fascination on the near future *in-situ* LIBS diagnostic in W7-X.

Acknowledgements

This work was supported by the National Natural Science Foundation of China (No. 11905049, No. 11875023, No.11904241), Department of Science and Technology of Sichuan Province (No. 2020YJ0181), the National Key R & D Program of China (No. 2018YFE0303101), Deutsche Forschungsgemeinschaft (No. 410415657), the Joint Sino-German Research Project (NSFC-DFG) and OPCP-Helmholtz postdoc fellowship. This work has been carried out within the framework of the EUROfusion Consortium and has received funding from the Euratom research and training programme 2014-2018 and 2019-2020 under grant agreement No 633053. The views and opinions expressed herein do not necessarily reflect those of the European Commission.

ORCID iDs

D. Zhao https://orcid.org/0000-0003-0387-4961
R. Yi https://orcid.org/0000-0002-4422-5178
A. Eksaeva https://orcid.org/0000-0003-4277-6766
J. Oelmann https://orcid.org/0000-0002-0845-4571
S. Brezinsek https://orcid.org/0000-0002-7213-3326
G. Sergienko https://orcid.org/0000-0002-1539-4909
M. Rasinski https://orcid.org/0000-0001-6277-4421
Y. Gao https://orcid.org/0000-0001-8576-0970
M. Mayer https://orcid.org/0000-0002-5337-6963
L. Cai https://orcid.org/0000-0002-7990-3282

References

[1] Liang Y. *et al* 2017 *Nucl. Fusion* **57** 066049
[2] Neubauer O. *et al* 2015 *Fusion Eng. Des.* **96** 891
[3] Dhard C. *et al* 2017 *Phys. Scr.* **2017** 014010
[4] Ruset C. *et al* 2009 *Fusion Eng. Des.* **84** 1662
[5] Dhard C P. *et al* 2019 *Fusion Eng. Des.* **146** 242
[6] Mayer M. *et al* 2020 *Phys. Scr.* **T171** 014035
[7] Sereda S. *et al* 2020 *Nucl. Fusion* In press
[8] Philipps V. *et al* 2013 *Nucl. Fusion* **53** 093002
[9] Semerok A, C Grisolia 2013 *Nucl. Instrum. Methods Phys. Res. Sect. A-Accel. Spectrom. Dect. Assoc. Equip.* **720** 31
[10] Imran M. *et al* 2019 *Surf. Interface Anal.* **51** 210
[11] Cai L. *et al* 2019 *Rev. Sci. Instrum.* **90** 053503
[12] Xiao Q. *et al* 2015 *J. Nucl. Mater.* **463** 911
[13] Zhao D. *et al* 2018 *Rev. Sci. Instrum.* **89** 073501
[14] Hubeny M. *et al* 2019 *Nucl. Mater. Energy* **18** 77
[15] Li C. *et al* 2017 *Phys. Scr.* **2017** 014004
[16] Oelmann J. *et al* 2019 *Nucl. Mater. Energy* **18** 153
[17] Zhao D. *et al* 2020 *Phys. Scr.* **T171** 014018
[18] Gao Y. *et al* 2019 *Nucl. Fusion* **59** 066007
[19] Pedersen T S. *et al* 2018 *Plasma Phys. Control. Fusion* **61** 014035
[20] Effenberg F. *et al* 2019 *Nucl. Fusion* **59** 106020
[21] Zhao D. *et al* 2020 *Fusion Eng. Des.* **151** 111379
[22] St-Onge L. *et al* 2002 *Spectroc. Acta Pt. B-Atom. Spectr.* **57** 1131
[23] Sattar H. *et al* 2019 *Plasma Sci. Technol.* **21** 034019
[24] Mateo M. *et al* 2006 *Surf. Interface Anal.* **38** 941
[25] Nagy T. *et al* 2017 *Appl. Surf. Sci.* **418** 508
[26] Yi R. *et al* 2020 *Appl. Surf. Sci.* **532** 147185
[27] Lazic V. *et al* 2018 *Spectroc. Acta Pt. B-Atom. Spectr.* **149** 1
[28] Mercadier L. *et al* 2011 *J. Nucl. Mater.* **414** 485
[29] Mateo M. *et al* 2001 *J. Anal. At. Spectrom.* **16** 1317
[30] Aberkane S M. *et al* 2018 *Thin Solid Films* **653** 293
[31] Margetic V. *et al* 2001 *J. Anal. At. Spectrom.* **16** 616
[32] Oelmann J 2020 *Forschungszentrum Jülich* Ph.D. thesis
[33] Eksaeva A. *et al* 2020 *Phys. Scr.* **2020** 014057
[34] Wang E. *et al* 2020 *Phys. Scr.* **2020** 014040
[35] Pintsuk G. *et al* 2009 *Fusion Eng. Des.* **84** 1525
[36] Bernard E. *et al* 2015 *J. Mater. Sci.* **50** 7031
[37] Gao Y. *et al* 2019 *Nucl. Fusion* **59** 106015